Estimation of Elastic Constants from 3D Range-Flow

Jochen Lang and Dinesh K. Pai

Laboratory of Computational Intelligence,
Department of Computer Science
University of British Columbia, Vancouver, B.C.
Canada V6T 1Z4.
e-mail: {jlang,pai}@cs.ubc.ca

Abstract

This paper shows how range-flow can help to estimate the elastic constants of complete objects. In our framework, the object is deformed actively by a robotic device pushing into the object. The robot senses the contact force and surface displacement at the point of contact. This contact object behavior alone is not sufficient to estimate elastic constants. The displacement of the object's non-contacted surface needs to be taken into account. This paper presents a method to estimate surface displacement from range-flow calculated with trinocular stereo imagery. The observed object behavior allows us to estimate the linear elastic material constants of the object. To this end we will introduce the boundary element method as a modeling tool for deformable objects in 3D imaging. The boundary element method is a full discrete continuum mechanics model.

1 Introduction

Realistic deformation of virtual objects are required in medical training simulators [5], in haptic interfaces for virtual worlds [6] and in design of robotic tasks involving soft materials [14, 15]. Biomechanical simulators can help to predict and plan some surgical procedures [8]. Many techniques have evolved over the years to model deformations for graphical rendering [11]. These techniques vary from full continuum models for elastic materials, include mass-spring particle systems to very ad-hoc methods. But even the most elaborate deformation model will be only as realistic as the match between simulated and physical material properties. The measurement of these material properties is commonly done in a "material oriented" way, e.g., by destructive testing in physical and mechanical testing laboratories. In contrast, this paper addresses the issue of acquiring elastic properties of complete objects.

In recent years, some solutions to the real-time simulation of linear elastic objects have been presented [13, 5]. In particular, James and Pai [13] have applied the boundary element method in interactive visual and haptics simulation of soft objects. However, the acquisition of deformable models for real objects is a major challenge. This paper shows how the boundary element method allows us to construct such models given the object geometry, a displacement and force field for the object. We measure the displacement field over the surface of the object by range-flow.

Range-flow is the task of matching depth information over time. The range flow constraint equation [12, 26] is the three-dimensional equivalent of the optical flow equation. Estimating range-flow is an even harder problem than optical flow because of the increased dimensionality. Nevertheless, there has been recent progress in range flow estimation [26, 24, 25], sometimes also referred to as scene flow [25].

Deformable models have been applied in computer vision in order to regularize the solution to shape and motion estimation of non-rigidly deforming objects [17, 20]. The role of the (physics-based) deformable model in these works is to facilitate the vision task at hand, and not to model the physical deformation at all. Typically, the forces in a regularization framework are associated with image data, while the elastic behavior of the model regularizes the influence of these noisy data onto the deformable model.

Our approach to calculating range-flow is a combination of simultaneous 2D-optical flow with stereo-depth information. This approach has been followed before [25, 27, 23], however, in our approach we utilize the redundancy of imagery to reduce the error in the very noise-sensitive optical flow. In this paper, we do not employ the boundary element method to regularize range-flow, rather we follow a purely local approach. We rely on the high quality cali-

bration of a commercial trinocular stereo system[1]. Because of the choice of stereo vision and optical flow we require objects to have sufficient visual texture. (Sufficient texture is texture which leads to an unique peak in the area-based correlation at the correct disparity in the stereo matching or at the correct location in the search area for optical flow.) We felt this to be of no great inconvenience since we are dealing with a (robotics) laboratory environment and most objects have either sufficient visual texture or visual texture can be added trivially. Also note that the deformable model derived with the boundary element method is independent of the method for calculating range-flow.

This paper outlines our general approach in Section 2. The equations for the deformable model are summarized in Section 3. Section 4 states our solution to the range-flow task and provide some evaluation of its performance. Finally, Section 5 gives results for a geometrically simple linear-elastic object and compares it with a simple standard destructive test.

2 Outline of Our Approach

The initial step in our approach is the acquisition of a geometric object model. The boundary element model utilized in our approach requires a watertight triangular mesh model. For some objects this model maybe readily available while for other objects such a triangular mesh will have to be generated from range measurements. Our active measurement facility, ACME [19, 18], allows us to acquire stereo range-data from varying viewpoints. The range-data is registered in object coordinates. The data may then be used directly in a surface reconstruction algorithm. Currently we employ software from the National Research Council of Canada to that end [22].

The ACME robotic facility allows us to position a rigid probe on the surface of the object. The probe is driven into the surface applying a force which is recorded together with the position of the probe. The global deformation of the object is observed with stereo-imagery from a calibrated viewpoint. This viewpoint can be either pre-calibrated with an optical target or calibrated on the fly with respect to the object, given that the object geometry constrains the registration task sufficiently.

We assume that the object is well approximated as a linear-elastic homogeneous isotropic material. The knowledge of the traction at the probe tip and displacements of at least two vertices are enough to estimate shear modulus and Poisson's ratio for the material of the object. In practice however, measurements are noisy and we apply a least squares estimation using all the vertices whose displacements we can observe.

[1]Our stereo-system is a Color-Triclops produced by Point Grey Research, Vancouver, Canada. (http:www.ptgrey.com)

3 Deformable Model

The deformable model is a *linear elastic map* between surface displacement u and surface traction p (force per area). The *linear elastic map* consists of the Green's functions of the boundary value problem associated with the object's elasto-static behavior. The linear elastic map can be derived from the boundary integral equation [7, 3]. We employ the well-known triangular linear boundary elements [9, 4] and choose the shear modulus γ and Poisson's ratio ν to represent the elastic constants of the material.

This section will quickly review the boundary element method for linear elasto-static bodies and show how it can be employed to estimate material properties. The notation follows the Einstein summation convention. All formulae are for the three-dimensional case with indices i, j and k ranging from 1 to 3. The indices are separated by comma for partial derivatives (e.g. $u_{i,j} = \frac{\partial u_i}{\partial x_j}$). Matrices are denoted with bold capital letters while vectors are denoted with bold lower-case letters.

Equation 1 is the boundary integral equation written as a weighted residual statement over surface Γ of the elastic body. The location of the load application is ξ, while the response location is χ and the distance between them is r (body forces, e.g., gravity, are ignored here but are straightforward to include). Coordinate i is associated with the point load, while j is the coordinate of the response. The weights of the equations, the terms $p^*_{ij}(\xi,\chi)$ and $u^*_{ij}(\xi,\chi)$, are Kelvin's fundamental solution for the 3-D Navier's equations for an infinite body with the same material properties subjected to an impulse point load. The fundamental solution can be separated into terms only dependent on geometry and terms only dependent on material constants (see Equation 2 and Equation 3; the surface normal is denoted by n).

$$\int_\Gamma u^*_{ij}(\xi,\chi)p_j(\chi)d\Gamma(\chi) = c_{ij}(\xi)u_j(\xi) + \int_\Gamma p^*_{ij}(\xi,\chi)u_j(\chi)d\Gamma(\chi) \quad (1)$$

$$p^*_{ij}(\xi,\chi) = \frac{1-2\nu}{1-\nu}\frac{r_{,i}n_j - r_{,j}n_i - \delta_{ij}\frac{\partial r}{\partial n}}{8\pi r^2} - \frac{1}{1-\nu}\frac{3r_{,i}r_{,j}\frac{\partial r}{\partial n}}{8\pi r^2} \quad (2)$$

$$u^*_{ij}(\xi,\chi) = \frac{3-4\nu}{\gamma(1-\nu)}\frac{\delta_{ij}}{16\pi r} + \frac{1}{\gamma(1-\nu)}\frac{r_{,i}r_{,j}}{16\pi r}. \quad (3)$$

Here the *Kronecker* delta, $\delta_{ij} = 1$ if $i = j; 0$ otherwise.

The boundary integral equation (Equation 1) can be derived from the static equilibrium condition $\sigma_{jk,j} + b_k = 0$

which states that the stress tensor derivatives $\sigma_{jk,j}$ (plus possibly some external forces b_j, e.g. gravity) have to be zero. The equilibrium condition is valid throughout the body of an object giving rise to a volume integral. This volume integral can be taken to the boundary through integration by parts (Green's theorem). Details on the derivation of the boundary integral equation can be found in many textbooks including [3, 9, 4].

3.1 Numerical evaluation

The integrals in Equation 1 can be numerically evaluated over linear triangular boundary elements with Gaussian quadrature. Linear triangular boundary elements approximate an object's surface by a triangular mesh and restrict the solution for the displacement and traction to linear shape functions over the triangular element.

In the following the traction vector field and the displacement fundamental solution tensor are written as $\mathbf{p}(\xi)$ and $\mathbf{u}^*(\xi,\chi)$ respectively. The left-hand side of Equation 1 at a mesh node l is

$$(\mathbf{Gp})_l = \int_\Gamma \mathbf{u}^*(\xi_l,\chi)\mathbf{p}(\chi)d\Gamma(\chi).$$

The traction vector field $\mathbf{p}(\xi)$ over the boundary is approximated with shape functions $\mathbf{p}(\chi) = \sum_{i=1}^{N} \hat{\varphi}_i(\chi)\mathbf{p_i}$ where $\mathbf{p}_i$ are the traction values at a node. Individual 3×3 block elements $\mathbf{G}_{lm}$ of the fundamental solution matrix are

$$\mathbf{G}_{lm} = \int_\Gamma u^*(\xi_l,\chi)\hat{\varphi}_m(\chi)d\Gamma(\chi).$$

The integrals are numerically evaluated by Gaussian quadrature. The computation is performed by a change to local baricentric coordinates for each element. The displacement vector field $\mathbf{u}(\xi)$ and the right-hand side are omitted here but are dealt with correspondingly. The discretized boundary integral equation is the matrix equation $\mathbf{Hu} = \mathbf{Gp}$. For a mesh with N nodes, the matrices $\mathbf{G}$ and $\mathbf{H}$ are of size $3N \times 3N$. The displacement vector at the nodes $\mathbf{u}$ and the traction vector at the nodes $\mathbf{p}$ are of size $3N$.

Separating the geometric and material properties terms as in Equation 2 and Equation 3, the overall matrix equation of the boundary element formulation is Equation 4.

$$\left[\frac{1-2\nu}{1-\nu}\mathbf{H_A} + \frac{1}{1-\nu}\mathbf{H_B} + \mathbf{C}\right]\mathbf{u} = \left[\frac{3-4\nu}{\gamma(1-\nu)}\mathbf{G_A} + \frac{1}{\gamma(1-\nu)}\mathbf{G_B}\right]\mathbf{p} \qquad (4)$$

$$\text{with } C_{ii} = (1-\delta_{ij})\left[\frac{1-2\nu}{1-\nu}H_{A_{ij}} + \frac{1}{1-\nu}H_{B_{ij}}\right]$$

Equation 4 allows for the estimation of material properties. The equation has to be rearranged for the specific boundary condition at hand. The prescribed traction and displacements are collected in $\mathbf{x}$ while the right-hand side is the complementary set of tractions and displacements. Exchanging elements in vectors $\mathbf{p}$ and $\mathbf{u}$ to yield $\mathbf{x}$ and $\mathbf{b}$ requires exchanging columns in matrices $\mathbf{G}$ and $\mathbf{H}$ to yield $\tilde{\mathbf{G}}$ and $\tilde{\mathbf{H}}$. The modified equation $\tilde{\mathbf{H}}\mathbf{x} = \tilde{\mathbf{G}}\mathbf{b}$ is solved with the Green's function matrix $\mathbf{A}$. The matrix $\mathbf{A}$ in Equation 5 is what we refer to as the *linear elastic map*. It is the product of the inverse matrix associated with vector elements in b times the matrix associated with vector elements in x.

$$\tilde{\mathbf{G}}^{-1}\tilde{\mathbf{H}}\mathbf{x} \;=\; \mathbf{A}\mathbf{x} \;=\; \mathbf{b} \qquad (5)$$

3.2 Estimation of Elastic Constants

Equation 4 and Equation 5 form the basis for our estimation technique. We select a boundary configuration in which the supporting surface is fixed, i.e., a displacement of zero is described and the free surface has its traction prescribed. This is the vector $\mathbf{x}$. In a probing step we apply some non-zero traction close to some vertex of the surface. The prescribed traction changes but not the boundary configuration which allows us to combine several probings. For each probing, we observe some part of right-hand-side vector $\mathbf{b}$. The observation at the probing location is the local measurement made with the robotic arm (Section 5) while the global deformation is observed by range-flow (Section 4).

We employ an iterative method to solve for shear modulus γ and Poisson's ratio ν. First, the surface integrals in Equation 4 are calculated. This is a very expensive computation ($O(TNM)$ with T the number of triangles, N the number of vertices and M the number of integration points), however, it needs to be done only once for a given triangular mesh. (It also has to be performed in any forward problem, e.g., when rendering the elastic response of the object.) We pick an initial guess for the unknowns γ and ν and calculate A. The objective function $F = (\alpha(\mathbf{Ax}-\mathbf{b}))^2$ is evaluated (α selects the observations made). We used the Matlab function *fmins*, an implementation of the Nelder-Mead simplex method, for the minimization task at hand. However, note that simpler methods should be sufficient because of the low dimensionality of the problem, the limited range of possible values for Poisson's ratio ν and the shear modulus γ acting like a scale factor. The single deformation objective function can be trivially expanded to multiple deformation in the same configuration. The vectors $\mathbf{x_1}\cdots\mathbf{x_n}$ and $\mathbf{b}_1\cdots\mathbf{b}_n$ are stacked vertically to form X and B, respectively. The $1\times N$ observation vectors $\alpha_1\cdots\alpha_\mathbf{n}$ are stacked horizontally to form matrix $\alpha_\mathbf{M}$.

4 Range-Flow

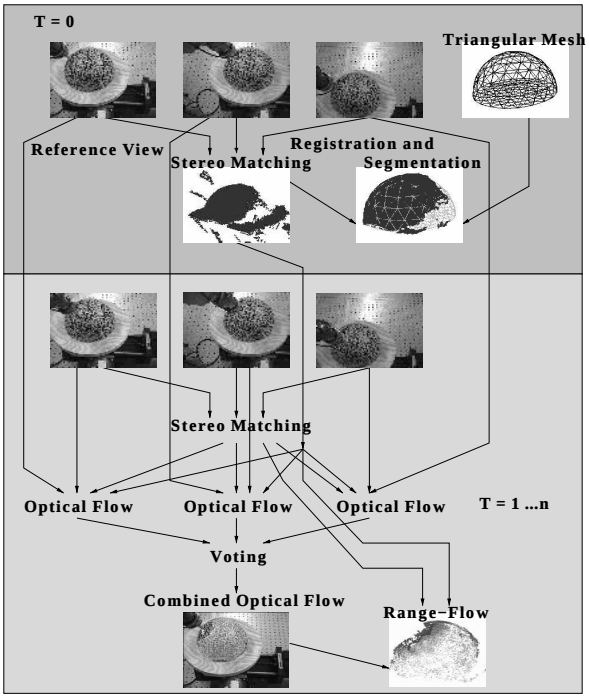

Figure 1. Range-flow processing: overview at T=0 (initialization) and T=1

Range-flow shown is at T=4; at T=1 there is no deformation since the probe is only just touching the object's surface.

We have developed a novel surface deformation measurement technique utilizing a trinocular stereo vision system. The technique tracks visual surface texture in three spatial dimensions, i.e., it calculates the range-flow of the deformable object's surface. The basic idea is to utilize the redundancy in the imagery provided by a trinocular stereo-system to increase robustness. We calculate optical flow with an area-based matching technique in all three cameras of the stereo-system. The disparity information is utilized to combine the optical flow results, as well as to add the third spatial dimension. In our approach, area-based matching is based on the normalized cross-correlation. We selected the normalized cross-correlation because of reports of its good performance in area-based matching [10] and because of its linearity with respect to pixel location. An overview of the range-flow calculation is shown in Figure 1. A geometric model of the undeformed surface of the object under test is either assumed known or acquired beforehand. This geometric model and the tracking capabilities of the system allow to segment the three-dimensional flow into surface flow and non-surface flow. In the following, we provide more detail on combining the optical flow results from the three cameras.

The images from stereo cameras are rectified such that the epipolar lines are aligned with the image axes. The result of the stereo processing with the *Point Grey Research Triclops* library is a triplet of row, column and subpixel disparity at each valid pixel in the reference image. A pixel is valid in our algorithm if the stereo processing produces a result and if the corresponding 3-D point is on the surface of the undeformed object. In order to decide if a point is on the surface, the 3D point-cloud is segmented and registered with the triangular mesh model of the object. We track the valid pixels in the reference image. The optical flow correlation scores are combined with the aid of stereo disparities. The from-pixel and to-pixel in the reference image are mapped with sub-pixel disparities into the stereo images, then the correlation between these locations is calculated (see Figure 1). Equation 6 expresses the normalized cross correlation of two image windows at column sub-pixel location given linear geometric image intensity interpolation. The window size is $2*n+1$. The correlation is specified for pixel a at location row r_a and column c_a plus $p = 0 \ldots 1$ and pixel b at location r_b and c_b plus $q = 0 \ldots 1$.

Assigning a confidence measure for optical flow results has been identified as a hard problem [1]. The integration of the results from all three stereo cameras into the reference camera frame allows us to reject outliers, especially if they are generated by viewpoint dependent effects (e.g., highlights) or the flow result is unstable because of the ambiguous correlation results (lack of texture, multiple motions, etc.). We apply a voting scheme and accept the result only if all cameras are in good accordance, i.e. the optical flow results from all stereo images have to be in the 8-neighborhood of the maximum correlation score. Our voting scheme rejects outliers rather than trying to find the correct flow. The robust optical flow techniques of [2] (multiple motions within an aperture) or the SSD-based regularization method of [16] (minimizing the effect of discretization errors in the flow) could be combined without our technique and should lead to denser results.

Because of the difficulty of obtaining ground-truth for surface deformation, we evaluated our range flow algorithm by tracking a moving rigid test object. We evaluated our method with an object translating and rotating. In Figure 2 the estimated optical and range-flow for the test object translating and rotating are shown.

Table 1 compares our range-flow result to the correct translational motion. The correct motion is obtained from reading back encoder values of high-precision linear positioning devices. The table shows the result for tracking the object over eight time steps plus one time step for initializa-

$$
\begin{aligned}
I_{corr}(r_a, c_a, r_b, c_b) &= \sum_{l=-n}^{n} \sum_{k=-n}^{n} \left[(I_{r_a+l,c_a+k} - \bar{I}_{r_a,c_a})(I_{r_b+l,c_b+k} - \bar{I}_{r_b,c_b}) \right] \\
CC(r_a, c_a, r_b, c_b, p, q) &= (1-p)(1-q) I_{corr}(r_a, c_a, r_b, c_b) + (1-p) q I_{corr}(r_a, c_a, r_b, c_b) \ldots \\
&\quad + p(1-q) I_{corr}(r_a, c_{a+1}, r_b, c_b) + pq I_{corr}(r_a, c_a + 1, r_b, c_{b+1}) \\
SCC(r_a, c_a, p) &= ((1-p)(1-p) I_{corr}(r_a, c_a, r_a, c_a) + 2.0(1-p) p I_{corr}(r_a, c_a, r_a, c_{a+1}) \ldots \\
&\quad + pp I_{corr}(r_a, c_{a+1}, r_a, c_{a+1}) \\
NCC(r_a, c_a, r_b, c_b, p, q) &= \sqrt{CC(r_a, c_a, r_b, c_b, p, q)^2 / SCC(r_a, c_a, p) / SCC(r_b, c_b, q)}
\end{aligned} \tag{6}
$$

tion. The tracking is initialized only with surface points in the initialization time step. Therefore, the number of points tracked decreases with each time step. The correlation window size is $7x7$ pixels with a search range of $13x13$ pixels. The motion between steps is $2.5mm$. We report the true and estimated values for the orientation and length of the 3D range-flow with respect to the initialization step. The reference camera of the stereo-head is $81.0cm$ away from the center of the object coordinate frame (which is a typical distance in our system to observe deformation from). Our method produces results for translation to about $\frac{1}{2}$ millimeter accuracy which is sufficient for soft deformation. The motion to the left-rear in the reference image (Table 1 (a)) produces better results than the motion to the rear-right (Table 1 (b)). We suspect this to be due to the specific dominant orientation of the intensity texture of the test object.

Table 2 summarizes the results for vertex displacement estimation, again for the same translation test and for a rotation test conducted in the same way. The rotation in each step is 2.0° to a total The vertex displacement is estimated as the weighted average of filtered motion close to a vertex (within $1cm$). The motions are filtered by least median estimation followed by $\geq 3\sigma$ outlier rejection. The remaining motion is weighted averaged with $1/(1+d)$ based on the distance d from the node. The error reflects both the error in the vertex displacement as well as an error in the initial registration of the surface. The error in the orientation is also due to the missing sub-pixel optical flow estimation. This can be seen from the improvement in orientation as the motion vectors become larger (especially in the orientation test). We have not yet implemented a sub-pixel step after the voting in the range-flow calculation, we suspect this to improve the orientation results significantly.

Finally, Figure 3 shows the range-flow estimated for a deforming object, a toy tiger.

5 Estimation Results

This section presents the results of our method on a test object: a half of a soft (Nerf^{TM}) ball. The estimation results for the half ball are summarized in Table 3. We will give further details on the estimation below. The linear elastic model is a good approximation for the ball and the model fitting is successful. The estimated parameters ν and γ, when used in simulation, produce results which closely resemble the recorded range-flow (see Figure 4).

The results in Table 3 are from measured displacements by range-flow and displacement and force at a probed vertex. The force at a probed vertex has to be converted into surface traction for the estimation. The observed force has to satisfy $f = \int_\Omega (p)$. The surface is represented as a triangular mesh and the shape functions for the tractions are linear. The force has to be the sum over all integrated traction shape-function on elements connected to the probed vertex, i.e. $f_i = \sum_j \frac{1}{6}(p_i^{1j} + p_i^{2j} + p_i^{3j})\,|J|$.

Table 3 also contains a comparison with a destructive test. The test is a simple compression test of a cylindical material sample. The material sample is compressed measuring force and the reduction in length of the cylinder. In practice, this works well for metal samples in common testing machines, however for soft elastic material it is far less precise. For our test object, the object behavior is greatly influenced by a membrane-like layer over its surface, i.e. the cylinder cut will have to have that membrane intact. For a compressed cylindical material piece the Young modulus is $E = \frac{Fl}{A\delta_l}$, where F is the compression force, l and δ_l is the height and the change in height of the cylinder, respectively, and A the area of its circular end (see e.g. [21]). For homogeneous isotropic linear-elastic material, the relation between shear modulus γ and Young's modulus E is $\gamma = \frac{E}{2(1+\nu)}$. This allows for the comparison in table 3, which shows an excellent correspondence between the material-based compression test and our complete object-based method. The variation of the estimates between single probes is mostly likely due to the misalignment of the probe with respect to the surface. Combining the measurement in one estimation step averages out the noise nicely.

A visual comparison between the measured displacement and the simulated displacement for a probing is shown

Angle $[deg]$		Length $[cm]$			
Mean	σ	Mean	σ	Encoder	Command
67.0081	10.2836	0.2678	0.0340	0.2355	0.2500
64.7748	5.7253	0.5396	0.0402	0.4864	0.5000
64.8529	4.1890	0.8113	0.0464	0.7374	0.7500
64.8575	3.5898	1.0849	0.0571	0.9911	1.0000
64.9783	2.8942	1.3567	0.0626	1.2378	1.2500
65.0915	2.6112	1.6290	0.0697	1.4867	1.5000
65.1626	2.3755	1.9019	0.0770	1.7366	1.7500
65.2725	1.9633	2.1747	0.0827	1.9929	2.0000

Angle $[deg]$		Length $[cm]$			
Mean	σ	Mean	σ	Encoder	Command
48.8813	7.4717	0.2367	0.0334	0.2230	0.2500
46.2486	4.5264	0.4926	0.0461	0.4750	0.5000
46.0249	3.3112	0.7404	0.0518	0.7146	0.7500
45.4467	2.6273	0.9997	0.0507	0.9729	1.0000
45.6313	2.6246	1.2471	0.0606	1.2161	1.2500
45.4051	2.5060	1.5086	0.0780	1.4705	1.5000
45.4808	2.4960	1.7614	0.0889	1.7192	1.7500
45.2843	2.3798	2.0266	0.0937	1.9736	2.0000

Table 1. Range-Flow Results for Translation
(a) Motion to the left-rear (b) Motion to the rear-right
The results are for the test-object in Figure 2. The reported 3D-angle is between the z-axis (optical axis) and the flow vectors. The variation in the angle decreases with greater translation while the variation in vector length increases with greater translation. The decrease in rotation indicates the influence of the discretization error in the optical flow. The increase in variation in the length of the flow vector is due to a reduction in the density of the flow-field combined with larger absolute flow values.

Translation in X		Translation in Y		Rotation around Z				
Angle $[deg]$		Angle $[deg]$		Angle $[deg]$		Length $[cm]$		
Error	σ	Error	σ	Error	σ	Mean	σ	Command
10.9142	23.2285	7.4402	15.0430	23.5574	47.8135	0.2998	0.0518	0.3053
8.6968	20.3784	5.8115	11.7741	24.8044	58.0988	0.5928	0.0884	0.6089
7.9037	18.9947	5.2960	10.6937	19.1940	42.1753	0.8739	0.1468	0.9052
8.0567	21.4754	5.0309	10.2249	17.5430	41.4193	1.1370	0.2130	1.2070
8.3435	23.5471	4.8527	9.9227	13.7172	37.8691	1.4744	0.2350	1.5336
8.0368	24.2161	4.8800	9.994	12.2357	36.0586	1.7621	0.3434	1.8643
8.1894	26.5517	4.9821	10.1555	10.0026	32.9437	1.9929	0.4729	2.1297
7.9706	28.0945	4.9916	10.1864	8.2385	31.2005	2.1469	0.6727	2.3233

Table 2. Node Displacement Results for a Translation and Rotation
The results are for the test-object in Fig. 2. Node displacements are the median-filtered weighted average 3-D flow within $1cm$ of a node (see text for details). The displacement are transformed into object coordinates. The errors are larger then in Table 1 since they are a result of both registration error and flow estimation error.

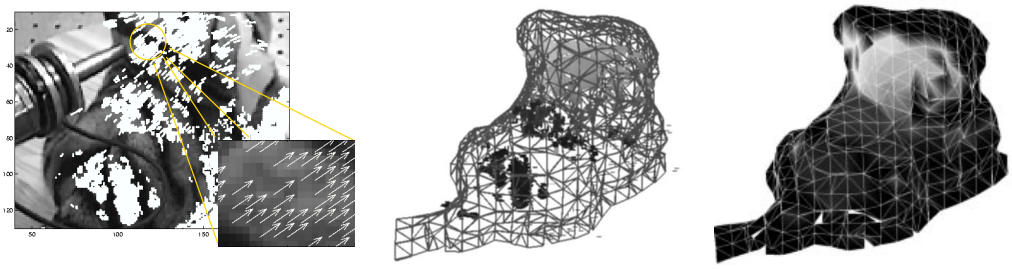

Figure 3. (a) 2D Optical Flow (b) 3D Range-Flow (c) Node Displacement
The 3D range-flow shows the distribution of the estimated flow vectors with brighter range-flow corresponding to larger motions. The node displacement figure also shows larger movement being brighter. Dark surface is either stationary or no estimate is available.

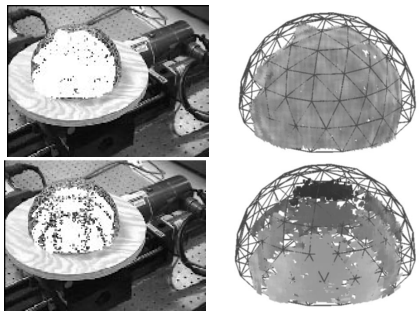

Figure 2. Optical Flow and Range-Flow
Tracked surface points during translation and rotation of a rigid test object. First row, translation by $5mm$, second row, rotation by 2.0 $^\circ$ deg. around the object's z-axis (up in the image). The optical and range-flows show the distribution of the estimated flow vectors. Brighter range-flow corresponds to larger motion.

Node No.	ν	γ	E
1	0.1183	0.7809	1.746
2	0.1878	0.6308	1.499
3	0.2227	0.6039	1.477
4	0.2516	0.6555	1.641
5	0.1857	0.6977	1.655
6	0.2009	0.6696	1.608
8	0.2089	0.6550	1.584
9	0.2007	0.6646	1.596
11	0.1868	0.7175	1.703
12	0.2082	0.7585	1.833
14	0.1997	0.7993	1.918
15	0.2084	0.7451	1.801
17	0.1192	0.7666	1.716
18	0.1366	0.7562	1.719
20	0.1400	0.7480	1.705
22	0.1264	0.7121	1.604
26	0.1442	0.9383	2.147
ALL the above	0.1730	0.7283	1.709
Test:	-	-	≈ 1.75

Table 3. Material Properties Estimation Results

The table lists the estimation results of the material properties (shear modulus γ, Poisson's ratio ν and the corresponding Young's modulus E) for the half-ball. Each row in the table contains the result for a separate estimation based on the force probe location at the specified node(s). Using data from all probes in a single estimation results in values for the material properties very close to an independent compression test for the material.

in Figure 4. The magnitude of surface displacement is in very good correspondence in the simulation and the measurement on the surface area not occluded by the probe.

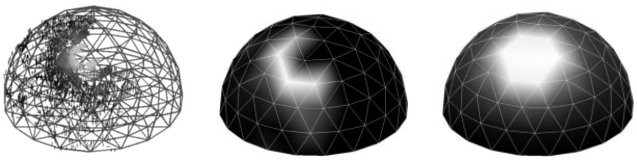

Figure 4. Comparison of Measured and Simulated Displacement

From left to right: 3D range-flow, estimated displacement, simulated Displacement.
The 3D range-flow shows the distribution of the estimated flow vectors with brighter range-flow corresponding to larger motions. The node displacement figure also shows larger movement being brighter. Dark surface is either stationary or no estimate is available. The estimated node displacement forms a partial ring around the location of the probe; the location itself and the other part of the ring are occluded by the probe.

6 Conclusion

This paper shows how elastic constants of complete objects can be estimated. The method combines 3D range-flow with a full continuum mechanics deformable model. The deformable model describes the elastic behavior of the object based on its surface geometry and material constants. In our method 3D imaging is employed to find the object's geometry and the object's material properties. We employ a purely local but robust range-flow technique for the measurement of surface displacements. We demonstrated the effectiveness of the range-flow technique in the estimation of elastic constants for a test object. Our on-going work focuses on more complicated models. It should be possible to increase the geometric complexity of our test objects with the described technique. However, we are also interested in modeling elastic behavior of objects which deviates from the homogeneous isotropic linear-elastic model. For such objects the estimation of elastic constants may not be reasonable, however directly estimating the Green's function would still enable applications in simulation, haptics and computer vision.

Acknowledgments

The financial support of the Federal Networks of Centres of Excellence IRIS project and NSERC Canada is gratefully

acknowledged. We thank D. James, Dr. R.J. Woodham and J.E. Lloyd for their valuable input to parts of this work.

References

[1] J.L. Barron, D.J. Fleet, and S.S. Beauchemin. Performance of optical flow techniques. *IJCV*, 12(1):43–77, 1994.

[2] M.J. Black and P. Anandan. The robust estimation of multiple motions: parametric and piecewise-smooth flow fields. *Computer Vision and Image Understanding*, 63(1):75–104, 1996.

[3] C.A. Brebbia. *Boundary element techniques in engineering*. Pentech Press, London, Uk, 1978.

[4] C.A. Brebbia, J.C.F. Telles, and L.C. Wrobel. *Boundary element techniques: theory and applications in engineering*. Springer-Verlag, Berlin, 1984.

[5] S. Cotin, H.Delingette, and N. Ayache. Real-time volumetric deformable models for surgery simulation. In *Visualization in Biomedical Computing*, volume 4, Hamburg, Germany, Sept. 1996.

[6] S.A. Cover, N.F. Ezquerra, J.F. O'Brian, R. Rowe, T. Gadaxz, and E. Palm. Interactively deformable models for surgery simulation. *IEEE Computer Graphics & Applications*, 13(6):68–75, 1993.

[7] T.A. Cruse. An improved boundary-integral equation method for three dimensional elastic stress analysis. *Computers & Structures*, 4:741–754, 1974.

[8] H. Delingette. Toward realistic soft-tissue modeling in medical simulation. *Proceedings of the IEEE*, 86(3):512–523, 1998.

[9] J. Dominguez. *Boundary Elements in Dynamics*. Computational Mechanics Publications, Southhamptom, Uk, 1993.

[10] P. Fua. A parallel stereo algorithm that produces dense depth maps and preserves image features. *Machine Vision and Applications*, 6:35–49, 1993.

[11] S.F.F. Gibson and B. Mirtich. A survey of deformable modeling in computer graphics. Technical Report TR-97-19, Mitsubishi Electric Research Laboratory, Cambridge, MA, USA, Nov. 1997.

[12] B.K.P. Horn and J.G. Harris. Rigid body motion from range image sequences. *CVGIP: Image Understanding*, 53(1):1–13, 1991.

[13] D.L. James and D.K. Pai. ArtDefo accurate real time deformable objects. In *SIGGRAPH*, Los Angles, Aug 1999. ACM.

[14] A. Joukhadar, C. Bard, and C. Laugier. Planning dextrous operations using physical models. In *International Conference on Robotics and Automation*. IEEE, 1994.

[15] A. Joukhadar, F. Garat, and C. Laugier. Parameter identification for dynamic simulation. In *International Conference on Robotics and Automation*, pages 1928–1933, Albuquerque, NM, USA, 1997. IEEE.

[16] S.-H. Lai and B.C. Vemuri. Reliable and efficient computation of optical flow. *International Journal of Computer Vision*, 29(2):87–105, 1998.

[17] D. Metaxas and D. Terzopoulos. Shape and nonrigid motion estimation through physics-based synthesis. *PAMI*, 15(6):580–591, 1993.

[18] D.K. Pai, J. Lang, J.E. Lloyd, and J.L. Richmond. Reality-based modeling with acme: A progress report. In *International Symposium on Experimental Robotics*, volume 7, Honolulu, USA, December 2000.

[19] D.K. Pai, J. Lang, J.E. Lloyd, and R.J. Woodham. Acme, a telerobotic active measurement facility. In *International Symposium on Experimental Robotics*, volume 6, Sydney, Australia, March 1999.

[20] A. Pentland and J. Williams. Perception of non-rigid motion: Inference of shape, material and force. In *Int. Joint Conference on Art. Intelligence*, volume 2, pages 1565–1570, Aug 1989.

[21] E.P. Popov. *Engineering mechanics of solids*. Prentice Hall, Englewood Cliffs, NJ, USA, 1st edition, 1990.

[22] G. Roth and E. Wibowoo. An efficient volumetric method for building closed triangular meshes from 3-d image and point data. In *Proc. Graphics Interface*, pages 173–180, 1997.

[23] H. Spies, B. Jähne, and J.L. Barron. Dense range flow from depth and intensity data. In *International Conference on Pattern Recognition*, volume 1, pages 131–134, Barcelona, Spain, 2000.

[24] H. Spies, B. Jähne, and J.L. Barron. Regularised range flow. In *European Conference on Computer Vision*, LCNS 1843/44, pages 785–799, Dublin, Ireland, 2000. IEEE, Springer-Verlag, Berlin.

[25] S. Vedula, S. Baker, P. Rander, R. Collins, and T. Kanade. Three-dimensional scene flow. In *International Conference on Computer Vision*, pages 722–729, 1999.

[26] M. Yamamoto, P. Boulanger, J.-A. Beraldin, and M. Rioux. Direct estimation of range flow on deformable shape from a video rate range camera. *PAMI*, 15(1):82–89, 1993.

[27] Y. Zhang and C. Kambhamettu. Integrated 3d scene flow and structure recovery from multiview image sequences. In *Computer Vision and Pattern Recognition*, volume 2, pages 674–681, 2000.